PCCP

Accepted Manuscript

ROYAL SOCIETY OF CHEMISTRY

www.rsc.org/pccp

Local strain effect on the thermal transport of graphene nanoribbon: a molecular dynamics investigation

Lanqing Xu,[a] Xiaoman Zhang[a] and Yongping Zheng [*b]

Strain engineering of the thermal conductivity of graphene is highly desirable for various nanoscale thermal devices. Previous investigations have been focused mainly on the uniform strain applied uniaxially or biaxially. In this work we investigated, by non-equilibrium molecular dynamics simulations, the thermal transport behavior of graphene nanoribbon under local, nonuniform strain. A capped carbon nanotube (CNT) is used as a representative tip to indent the graphene, which creates a local stress field similar to those that induced by nanoindentation or molecular adsorption. The relations among structural deformations, phonon transport, and stress field were analyzed, and the effects of indentation depth, tip-surface interaction strength were discussed. More than 50% reduction of thermal conductance can be observed for a 20 nm$\times$ 5 nm graphene nanoribbon under indentation. Our study revealed that the thermal transport of graphene responds flexibly and sensitively to the local strain, which can be exploited for new functional nanodevices across various disciplines such as position sensing or molecular sensing. Thermal sensor based on graphene can then be constructed.

1 Introduction

As one of the most high-profile materials in current nanotechnology research, graphene has brought countless opportunities to explore new physical phenomena and to implement novel devices. Owing to its extraordinary electronic properties [1], superior mechanical strength [2] and ultrahigh thermal conductivity [3,4], graphene has been suggested as an ideal candidate in the applications for electronic and thermal management devices.The thermal conductivity of suspended graphene varies in the range from 1800-5000 W/m·K depending on the sample size and quality [3,5–8]. The thermal conductivity of supported graphene is reduced to the range 370-660 W/m·K due to phonon scattering on the substract [3,7,9]. Moreover, the thermal properties of graphene are sensitive to small perturbations. For example, the change from 0.01% to 1% in C^{13} isotope content reduces the thermal conductivity of graphene at room temperature by approximately 25% [8]. The quality of the contacts between graphene and substrates can influences heat transfer significantly as well [10]. Other theoretical investigations involving *ab initio* calculations and molecular dynamics (MD) simulations also revealed that κ varies with size, temperature, chirality, and defects, etc [11–13].

Being a very stable atomically thick membrane that can be suspended between two leads, graphene provides a perfect platform for desirable thermal management applications in various disciplines such as thermal waveguides, switches, rectifiers, thermal transistors, thermal barriers, and thermoelectrics [3,4,14,15], wherein materials with high/low, isotropic/anisotropic, even variable thermal conductivities are required to realize functions or to simplify the design. Chemical decoration, such as hydrogen functionalization has been revealed to tune κ of graphene effectively over a wide range via defect ratio engineering [16]. By physically tailoring graphene nanoribbon into asymmetric shapes such as triangle [17], direction-dependent thermal rectification can be obtained. Moreover, to utilize the giant contrast of κ between the in-plane and out-of-plane directions, molecular or carbon-based interlayer cross-links were added to quantitatively control the thermal conduction across the graphene layers. Via structural designs [18,19] of its carbon backbone, selective thermal transport can be achieved effectively.

Apart from the aforementioned aspects, strain is also known to drastically affect heat transport when introduced in an otherwise undisturbed crystalline lattice. Strain in silicon is now a major engineering tool for improving the performance of devices, and is ubiquitously used in device design and fabrication [20,21]. Thermal conductivity of single-wall CNT can be tuned flexibly under both compressive and tensile axial deformations [22,23]. Thermal conductivity of graphene is also very sensitive to strain. Thermal conductivity of suspended single layer graphene can be reduced by both compressive and tensile strain [24]. Nonuiform strain field on the graphene nanoribbon can induce asymmetric heat transfer and significant thermal rectification over 70% can be achieved [25]. In a multilayer grephene stack, with a compressive cross-plane stress of 2 GPa, the Kapitza resistance is reduced by about 50%. On the other hand, compressive in-plane strain can either increase or reduce the Kapitza resistance, depending on the specific way it is applied [26]. Computational study showed that graphene sheets undergo complex reconstructions when the strains were applied, which induced variations in thermal conductivity [27]. The suggested strong strain dependence of the thermal conductivity for graphene can explain some of the

[a] *Key Laboratory of OptoElectronic Science and Technology for Medicine of Ministry of Education, Fujian Normal University, Fuzhou 350007, China.3*
[b] *College of Physics and Energy, Fujian Normal University, Fuzhou 350007, China. Fax: 86-0591-8346537 E-mail: zyp@fjnu.edu.cn*

discrepancies in the reported experimental values. More profound first-principles calculation of lattice vibrations showed that under tensile strain the two degenerate optical branches in the phonon dispersion curves split near the G points, and the frequencies of the optical phonon modes shift down. With a strain exceeding a threshold of 16% a frequency gap was observed which forbids vibration modes in the frequency region. High-frequency phonon modes shift down discernibly, more phonons are activated and the heat capacity is increased, κ is reduced because of enhanced Umklapp scattering among more phonons[28]. Other physical characters, such as the acoustic phonon lifetime, were also revealed to be closely related to strain[29]. Thermal transport of graphene under strain has attracted significant attentions over the past decade.

Through literature review we found that previous reports have been focused mainly on the effect of uniform strain applied, limited attention has been paid to the local strain or nonuniform structural deformation[25]. Local, nonuniform strain is frequently encountered during material test or fabrication. Molecular adsorption and nanoindentation are the two most common ways to induce local stress field. It has been clarified that local stress field created by probe-tip (such as atomic force microscopy tip) can lead to a spatially confined quantum dot on the graphene sheet, resulting in completely different electronic spectrum[30]. Mechanical properties can also response sensitively to the exerted strain. These kinds of variations can be used to design electric sensors[31], mass sensors[32], strain sensors[33], molecular sensors[34,35], etc. But how can the heat transfer be affected by an approaching/retracting indenter tip or an adsorbed molecule? What are the effects of the interaction strength between the tip/molecule and the graphene surface on the heat transfer?

There are two general issues among these questions: (1) the approaching of indenter tip or the adsorption of a molecular can induce a local deformation region which can trigger phonon scattering and hence influence heat transfer; (2) different kinds of tip/molecular will have different interaction strength, which can superimposes on the effect from stress-induced local deformation. Up to now little is known on the thermal response of graphene under local strain, not to mention the corresponding applications. The vast knowledge gained so far invites deep understanding of this point. To this end, in this work we performed molecular dynamics (MD) simulations to investigate the thermal transport behavior of graphene nanoribbons under local strain. The strain is applied via nanoscale indentation, a method which is usually applied to test the mechanical properties of materials in small dimensions[36]. Focus is placed on the heat blocking and phonon scattering on the graphene plane beneath the indenter tip, and the underpinning mechanism was discussed.

2 Models and methods

2.1 Models

We used a representative capped CNT to indent a graphene nanoribbon (GNR), as illustrated in the lower inset in Fig. 1. The size of the GNR investigated is $230\mathring{A} \times 50\mathring{A}$. An edge region of $\sim 5\mathring{A}$ at each end of the longitudinal direction (x-axis) is fixed to ensure that the sample will not move downward during indentation. Beside the fixed region is the thermobath with a width of 10 $\mathring{A}$, which is large enough to maintain a robust heat flux. Thus, the effective length of the ribbon is 20 nm. A capped CNT is used to simulate the tip or testing molecule and approaches the graphene surface from the center of the GNR, resulting in a local indentation region beneath the tip. The depth of the indentation can represent the approaching depth or the position of tip/molecular, and the varying interaction strength can be simulated via tuning the Lennard-Jones (L-J) coefficients between the CNT and the GNR due to the non-bonding character. Herein, we define the indentation depth as the distance between the tip and the graphene basal plane (see the upper-right inset in Fig. 1). Positive depth corresponds to indentation and negative depth represents retraction of the tip.

2.2 Computational methods

MD calculations are carried out using LAMMPS software package[37], and the bonding and non-bonding atomic interactions are expressed by the widely used AIREBO potential[38] and the L-J potential, respectively. A vacuum space of 10 $\mathring{A}$ is inserted in both the lateral direction (y-axis) and the vertical direction (z-axis). The capped CNT approaches the graphene surface to a certain degree to ensure a firm contact, and then approaches deeper or retracts away to simulate various indentation depths. After that, the tip is fixed during the whole simulation. Initially, 200 ps Nóse-Hoover thermo bath coupling[39] (coupling constant 0.1 ps) with background temperature 300 K are conducted to achieve equilibrated structures. The structural optimization was performed using the Polak-Ribière version of the conjugated gradient algorithm. The Velocity-Verlet time stepping method is adopted and the integration time step is set as 0.5 fs. After the equilibrium state was achieved, NVE ensemble is adopted and non-equilibrium molecular dynamics (NEMD) simulations are performed to investigate the thermal transport behavior. The imposing of heat flux is realized by the energy and momentum conserving velocity rescaling algorithm[40], which has been widely used to investigate asymmetric heat transfer in various materials[41]. By rescaling the atomic velocities at specified time interval dt, a specific amount of kinetic energy dE is injected into the source and subtracted from the sink respectively. Thus, a temperature gradient can be set up. The imposed heat flux can be calculated as $J = dE/dt$. After 2.5 ns of the exchanging process

the nonequilibrium steady state is reached, and the subsequent nonequilibrium simulation process covers 3 ns. To calculate the thermal conductivity, we divide the GNR into several slabs of constant length of 2 $\AA$ along its axis. Within each slab the instantaneous kinetic energy is used to compute the temperature and the obtained momentary temperature is averaged over a 3 ns time interval to calculate the temperature profile, that is

$$T_i = \frac{1}{3N_i k_B} \sum_{j=1}^{N_i} m_j v_j^2 \tag{1}$$

where N_i is the number of atoms in the i^{th} slab, k_B is the Boltzmann constant, m_j and v_j represent the mass and velocity of the atom j, respectively. The temperature profile of a typical indented GNR sample, along with the schematic of atomic configuration and the corresponding heat source and sink domains, are presented in Fig. 1. According to the Fourier's law, the thermal conductivity can be calculated by

$$\kappa = \frac{J/A}{\partial T/\partial x} \tag{2}$$

where A is the cross sectional area in the heat transfer direction, which equals the product of the width and thickness of the ribbon. The thickness of graphene is assumed to be 0.142 nm, which is the generally accepted C-C bond length and has been repeatedly used in literature to obtain thermal conductivity of graphene or CNTs[22,27]. We examined a zigzag graphene nanoribbon of $200\AA \times 50\AA$ and obtained a thermal conductivity of 253.1 W/(m·K), which fits well in the κ range of previous reports[17,18,22,27] and confirmed the validity of the simulation methods used here. The thermal conductivity of graphene calculated by the NEMD method increases with increasing sample size. However, in this work we focus on the relative variation of thermal conductivity with respect to indentation. Different sample lengths lead to different predictions of the indent deformation for a given relative reduction of thermal conductivity, but the overall decreasing trend of thermal conductivity upon indentation is not affected by the finite-size effects, as will be discussed in Section 3.4.

For further analysis, we also calculate the phonon spectrum function (phonon density of states) $g(\omega)$ as a function of the phonon frequency ω from Fourier transform of the velocity autocorrelation function[42]:

$$g(\omega) = \frac{1}{\sqrt{2\pi}} \int_0^\infty e^{i\omega t} C_{vv}(t) dt, \tag{3}$$

where the normalized velocity autocorrelation function $C_{vv}(t)$ is defined to be

$$C_{vv}(t) = \frac{\langle \sum_n \mathbf{v}_n(t_0+t) \cdot \mathbf{v}_n(t_0) \rangle}{\langle \sum_n \mathbf{v}_n(t_0) \cdot \mathbf{v}_n(t_0) \rangle}. \tag{4}$$

Here, $\mathbf{v}_n(t)$ is the velocity vector of atom n at time t, the summations are over the atoms in the relevant part of the simulated system and $\langle\ \rangle$ denotes ensemble averaging over different time origins t_0. The above definition corresponds to the total phonon density of states. However, we are also interested in its x, y, and z components, which are calculated by using the corresponding components of the velocity vectors. In our calculations, the velocities were recorded every 1 fs and the ensemble averaging was performed over a time interval of 50 ps after the system reaches equilibration.

3 Results and discussions

3.1 General temperature profiles

We first investigate the general temperature profiles of a pristine GNR and an indented GNR (Fig. 1). The temperature profile of pristine GNR is a typical figure which had also been shown up in other existing works[43]. The boundary temperature jump near thermobath is claimed to be induced by edge states of the system[44]. Thus, care must be taken while calculating κ from this non-linear profile which indicates that thermal transport is not fully diffusive. To avoid edge effects and to obtain correct diffusive κ we use the temperature gradient of the middle portion (linear part) between the thermobaths, and the obtained κ is 253.1 W/(m·K) for pristine GNR. The calculated κ in our samples are much smaller than the reported values for isolated monolayer graphene ($\sim$ 1800-5000 W/(m·K))[5–8], given the finite size of our simulated system wherein size effects will play. However, one is still able to observe changes in thermal transport caused by structural deformation even when the simulation size is not large[22,43]. As will be seen in the following sections, this sample size is also large enough to demonstrate the impeding of heat transfer owing to local structural deformation.

Upon indentation, the sheet beneath the tip was pressed down, leading to stretched C-C bonds and a bowl-like local structural deformation. Structurally, the honeycomb lattice is still well maintained and no Stone-Wales defect or vacancy defect as reported elsewhere[45] was found. Thus, no significant corrugation was observed. The appearance of indenter tip perturbs the heat flow on the graphene plane, as can be surmised from the slightly disturbed temperature profile in Fig. 1. The temperature gradient is noticeably higher, resulting in a much smaller κ of 227.5 W/(m·K) with an indentation depth of 10 $\AA$. The structural deformation beneath the tip induces local strain which affects the vibration properties of the material. Speed of sound, frequency range, scattering rates, and therefore thermal conductivity are all altered, thus hinders heat transfer.

3.2 Effects of indentation

3.2.1 Local stress field To explore the origin of reduced heat conductance at the presence of indentation, we first investigate the stress distribution. The stress tensors for each individual carbon atoms are calculated[46,47] to obtain the spatial atomic stress distribution, and the noise is reduced by averaging the results over a period of 0.5 ps. From the obtained results (the lower inset in Fig. 2) one can see that the highest stress occurs among atoms beneath the tip, i.e., region A. A naive deduction is that the tip imposes high local stress on region A and confines atoms' vibration, therefore induces phonon scattering and hinders heat transfer. However, the vertical deflection profiles give rise to different answer. We focus on the carbon atoms under the indenter, i.e., atoms within the same y coordinate range of the indented CNT. The z coordinates of these atoms are first averaged along y axis to derive an instantaneous averaged $\underline{z(x)}$, and then averaged in the time span to derive the overall $\overline{z(x)}$. The standard deviation can be used to measure the degree of out-of-plane oscillations for atoms at different x position. From Fig. 2 one can see the lowest z occurs at the indent position ($x \sim 10$ nm), coinciding with the high stress field observed in region A. However, the local stress field does not confine the oscillation of carbon atoms. Atoms in the indented region (region A) oscillate much more severely than atoms in the other regions (region B), as represented by larger error bars or higher dz ($\sim 0.66\mathring{A}$ vs $\sim 0.37\mathring{A}$). Since this is quite counter-intuitive, we off-set the indenter to x = 6.5 nm and plotted $\overline{z(x)}$ as the grey curve. It is clear that the position of the largest error bar moves in accordance with indent position. The larger oscillation is caused by the indentation. To understand this point, we compared the atomic fluctuations over the whole ribbon and found that the most severe oscillation occurs at the edges. When the free, unconstrained edges meet the confined indented region, significant structural deformations occur, leading to severe fluctuations at the edge under the indenter. Driven by this, the atoms under the indenter fluctuate much more drastic than the atoms away from the indenter. Therefore, the point indenter induces significant structural deformation beneath the indenter which does not confine the atomic movement but promote it instead. We had also replaced the indenter with a CNT lying across the graphene, the fluctuations under the indented CNT were confined, but heat transfer was hindered at the indented region as well(Fig. A1).

3.2.2 Phonon density of states To further investigate the relation between the reduced heat conductance and the local deformation field, we selected three typical regions A, B, C (as illustrated in the inset snapshot in Fig. 3) and calculated their respective phonon spectrums and compared them with the pristine situation. Fig. 3(a) shows representative phonon spectrum for pristine GNR, exhibiting the typical G-band peak characteristic of vibration modes for 3-fold carbon atoms. However, phonon spectrums for region A, B, and C are quite different to each other, which suggests mismatched group velocity v_g and will leads to disturbed heat transfer across the overall sheet plane. This is the first point in understanding the decrease of κ. On the other hand, the phonon DOS for region A possesses two main characters that can affect heat transfer: the remarkable softening and broadening of G-band (Fig. 3 (a)). The broadening of the phonon modes indicates a descending of the life time of the corresponding modes[48]. As a result, their contributions to the thermal conductivity will be reduced. The softening of the higher frequency peaks will slow down the phonon group velocities and result in a thermal conductivity decrease according to the classical lattice thermal transport theory $\kappa = \Sigma_m C_v v_m l$, where C_v, v_m and l are the specific heat, group velocity and mean free path of the phonon, respectively. Similar softening of G-band was observed in the Raman spectra of graphene flake under uniaxial strain[49] and in few-layer graphene sheet under uniform in-plane strain[26].

To confirm the relation between the indentation and the softening, we calculated the phonon spectrums for atoms in region A of GNRs with 10 $\mathring{A}$ and 17.5 $\mathring{A}$ indentation depths(Fig. 3(b). It is interesting to observe that the G-band peak shift to lower range for deeper indentation ($\sim$ 49.5 THz for 10 $\mathring{A}$ indentation and $\sim$ 47.5 THz for 17.5 $\mathring{A}$ indentation). When the indentation is severe, G-peak splits into dual-peaks (due to the breaking of the double-degeneracy of the in-plane phonons[26]). From a comparison of Figs. 3(a) and 3(b) we can see that although the red-shift of G-band is obvious, the low frequency modes do not have significant band-shift. The contributions to the high and low frequency bands come from different donors. To understand this point, we recorded the velocities in x, y, z directions for atoms in region A and did Fourier transform to their VACFs. From the obtained results as presented in Fig. 3(c) one can see that the contribution to the high frequency bands ($>$ 40 THz) comes mainly from the x and y components of vibration modes, whereas the contribution to the low frequency bands comes mainly from the z component. Detailed analysis of the phonon modes with respect to indentation depth reveals that G-band exists only in the x and y components and they are shifted down as indentation goes on, and a small peak at $\sim$ 50 THz emerges and shifts down with increasing indentation for the z component (Fig. A2). The contributions to the G-band shift from the x and y components are much larger than the z component. Although the stress was applied from cross-plane direction, the structural confinement at the ribbon ends transfers the stress to couple with in-plane deformation, thus affected the in-plane phonon spectrum. The phonon spectrum analysis elucidates how cross-plane strain can be used to modulate the in-plane vibration and to affect the thermal transport.

From Fig. 3 one can see that the phonon spectrum in the low frequency range does not change significantly, which is

partly due to the boundary cut-down effect. To understand this point in more detail, lattice dynamics calculations are performed and the dispersion relations of strained graphene (uniform inplane strain $\varepsilon = 2\%$) are compared to the un-strained ones (Fig. 4). Herein periodic boundary condition is applied and the sample is strained biaxially and uniformly. It is worth pointing out that the out of plane movement of graphene atoms gives rise to flexual acoustic (ZA) and flexual optical (ZO) modes. ZA modes are expected to be the main heat carrier in graphene. With strain applied, a linearization of the dispersion relation of the ZA mode is observed. This kind of linearization suggested that nonvanishing group velocity for the ZA modes tend to propagate along the strain axis[50]. The in-plane acoustic modes, TA and LA, are slightly softened. The optical phonons in the high frequency range are softened significantly, leading to red-shifted G-band as observed in Fig. 3. In the point-indentation situation, stresses are accumulated under the indenter. The boundary around highly-stressed region induces group velocity mismatch and provides extra scattering channels to limit heat transfer, especially for the high frequency modes. Although the low frequency phonons may contribute more to the thermal conductance, in this point-deformation case the high frequency modes contribute much more to the transformation of the phonon spectrum than the low frequency modes.

3.2.3 Bond length analysis Phonon vibrations have close relation with bonds. To explore the underpinning mechanisms of the shifted phonon bands, we calculated the average bond length $\overline{L_{bond}(x)}$ as a function of x position for the middle portion of the ribbon (illustrated by the black rectangle in Fig. 5(a)). The obtained $\overline{L_{bond}}$ fluctuates around 1.407 $\AA$ over the majority of ribbon, whereas increases dramatically to 1.420 $\AA$ when the averaging region approaches the tip location ($x \sim 10$ nm), wherein the highest atomic stress exhibits (Fig. 5(b)). Thus, a strong bond-length mismatch will occur near the indenter tip. with increasing indentation depth, the mismatch becomes more and more severe(Fig. 5(c)). The abrupt mismatch between Region A and the surroundings behave like a grain boundary or a structural interface on the graphene plane. In the non-harmonic region, the enlarged lattice reduces the force constant. The mismatched bond length reduces the crystal symmetry. More phonons are activated and the Umklapp scattering effect would be more prominent. One can deduce that the stress field beneath the tip induces local bondlength stretching over region A under the tip, the strong phonon scattering at the mismatched boundary edge of region A confines the transfer of phonon modes, which finally leads to red-shifted G-band and hinders heat transfer. The disturbing of heat transfer will be more severe in the heavy load/deep indentation circumstances, as will be seen in the following discussion.

3.3 Effect of Tip-surface Interaction

The tip-surface interaction strength can have strong influence on the heat transfer. To further understand this point, we replaced the capped CNT with a tip of specific element and modeled tip-surface interaction using L-J description. By changing the L-J interaction strength one can simulate various kinds of tips. For simplicity we tested three elements (C, O, and Au) and an artificial element with varying strength ε. A summary of these interaction coefficients is given in Table 1. The inset snapshots in Fig. 6 illustrate the general structural deformation as ε increases, i.e., more adhesion surface between the tip and GNR upon larger ε. When the adhesion is significant, a ripple-like structural deformation can be observed, leading to a "boundary" between the indented region (beneath the tip) and the others. The upper-right inset in Fig. 6 illustrates a typical temperature profile, wherein a sharp temperature jump occurs at the indent position, which is similar to those temperature jumps observed at the grain boundaries[51,52] and crystal interfaces[53]. The jump in the temperature across the boundary gives a measure of the boundary conductance (Kapitza conductance) G through the relation $G = \frac{\langle Q \rangle}{\Delta T}$,where Q is the heat flux density and the brackets $\langle\rangle$ indicate the average of the quantities over time as well as over the particles in the sample. The calculated Kapitza conductance for Au tip at 10 $\AA$ indentation depth is 8.34×10^{10} W/(m^2·K), which is 80, 50 and 20 times larger than the boundary conductance reported for boundaries in Si-Si(001) $\sum$29 grain boundary[54], the Si-Ge $\langle 100 \rangle$ interface[55], and Si-Ge nanocrystal boundaries[53] respectively. With increasing ε the Kapizta conductance decreases exponentially. For C-C interface the obtained Kapizta conductance is estimated to be more than 1×10^{12} W/(m^2·K). The boundary mismatch observed here is more similar to the thermal boundary reported in Si-Ge nanocrystal boundaries[53] than the structural interface such as grains[51], wherein the temperature jump is not sharp and abrupt. Moreover, the boundary mismatch enhances with increasing indentation depth, the Kapitza conductance can increases under tight indentation and decreases under heavy indentation. Overall, strong tip-surface interaction can lead to greater temperature jump in the indented region and higher thermal resistance occurs wherein, and the boundary mismatch is enhanced upon deeper indentation. The indentation-induced "boundary" causes group velocity v_g mismatch and triggers strong phonon scattering, thus worsen the thermal transport.

3.4 Effect of indentation depth

Through the approach and retract cycle, the indenter can press the sheet surface to a certain degree, or lift the sheet plane over its normal height due to the van der Waals interlayer adsorption. To give more insight into the effect of indentation on the

heat transfer, we performed calculations on the thermal conductivity of GNRs with varying indentation depth. Firstly, the capped CNT indents into the GNR 2 $\AA$ below the surface plane to ensure a firm contact. Then, it indents further (to simulate the approaching process) or retracts backward (to simulate the retracting process), corresponding to positive or negative indentation depth respectively. With deeper indentation, the stronger local stress field leads to more severe bond mismatch and the phonon scattering is more significant. Thus, κ decreases quickly with increasing indentation depth (Fig. 7 (a)). The phenomenon in the retracting procedure is much more complicated. From the inset snapshots one can see that when the tip is lifted $1 \sim 2$ $\AA$ above the graphene basal plane, adhesion between the tip and graphene is strong and the graphene sheet is adsorbed upward as the tip retracts, resulting in a ripple-like deformation. The adhesion becomes weaker as the tip retracts on and disappears when the tip height is ~ 3.5 $\AA$ above the graphene basal plane, which indicates that there will be barely no interaction between the tip and the graphene surface. Similar effective interlayer interaction distance has been reported for AFM tip and graphite surface[56]. The variations of thermal conductivity with respect to d coincide with the observed structural deformation rules. The averaged κ begins to decrease from $d \sim -3.5$ $\AA$, wherein the tip-surface interaction begins to take effect. Although the standard deviation is large, the trend is still obvious. The small reduction of κ upon the lifting of the graphene sheet can be ascribed to the interlayer adhesion induced structural deformation.

In addition, thermal conductance C, defined as the time rate of steady state heat flow through a unit area of a material, provides another easy mean to measure in the experiments. Fig. 7 (b) illustrates the thermal conductance of indented GNR with different indentation depth. One can see that the thermal conductance of pristine GNR is around 5.70×10^9 W/(m^2·K). When the indenter approaches the graphene plane, the thermal conductance descends with enhanced indentation depth. The overall drop of C is more than 50% given 40 $\AA$ indentation. The huge drop of thermal conductance can be detected from the experimental point of view. More over, some previous studies showed that thermal conductivity of graphene deverges in the uniformly strained condition[50] and have a logarithmic devergence with respect to sample size[13]. We calculated κ and C for indented GNRs from 10 nm to 40 nm (Fig. 8). The indentation depth was kept as 15 Å. Both κ and C are reduced, and the absolute amounts of reduction vary with GNR size. However, the relative reduction percentages, κ/κ_0 and C/C_0, show a decreasing trend with increasing size and saturate when the ribbon length is $>$ 30 nm. Longer GNRs need to be indented to a larger depth to achieve the same degree of thermal variation, i.e., longer GNRs corresponds to lower sensitivity. Within the investigated size range, the point indentation have significant impact on the thermal transport which can be detected from the variation of κ or C, but different size of GNR will has different sensitivity. In turn, for a GNR with finite size, the indentation depth can be retrieved from the relative reduction of κ or C with proper calibration.

3.5 Further remarks

As stated in the Introduction, in this work we are concerning on two issues: (1) the effect of local deformation on the thermal transport; (2) the effect of tip-surface interaction on the thermal transport. Results in Section 3.2 addressed the first issue. The adhesion/indentation of tip/molecular induces localized high stress field beneath the representative indenter tip. However, the effect of local stress field on the thermal transport does not lie in the confinement of atomic vibrations. The stress-induced abrupt boundary mismatch and corresponding phonon scattering is the main reason. Results in Section 3.3 addressed the second issue. Different molecular/indenter tip can have different interactions with the graphene sheet. The interaction strength can affect the Kapitza conductance significantly. This gives us a hint to explore the application of thermal conductance in molecular sensing. Moreover, thermal conductivity and thermal conductance of graphene nanoribbon is very sensitive to the tip-surface distance. Within the van der Waals interaction range ($\sim 3.5\AA$), the tip begins to affect the structural conformation of graphene surface. The lifted surface can have a subtle influence on thermal transport, which can be utilized for non-contact molecular sensing or position sensing. With further indentation, κ versus indentation depth presents a nearly linear decreasing trend within the investigated strain range. And the variation of thermal conductance is large enough for an experimental measurement. Although other theoretical investigation showed that phonon thermal transport is largely unaffected by 1% strain[57], the investigated strain is applied uniformly within basal plane and the magnitude is rather small, which is quite different from the one investigated here. Regarding the divergence of thermal conductivity of graphene under strain and with size[13,50], our size test showed that within the investigated size range the rules of thumb exist as well with the exception that different size will have different sensitivity. In a broader view, the results as presented in Section 3.3 and 3.4 suggest that with proper calibration, the flexible variation of thermal transport of graphene under local strain can be utilized to construct sensitive molecular sensor and position sensor.There can be other effects which can also influence the thermal transport. In this work, we focus on the indentation, leaving complications of coexistence of defect scattering for a possible future study.

4 Conclusions

In summary, in this work non-equilibrium molecular dynamics simulations were conducted to investigate the thermal transport on graphene under local strain. The strain was applied via using a representative capped CNT to indent the graphene nanoribbon. Significant structural deformation was observed beneath the tip, and the conformation is disparate for different tip-surface distance and tip-surface interaction. The abrupt structural changes exhibit themselves clearly and flexibly in thermal conductivity, thermal conductance and Kapitza conductance, i.e., unusual heat transfer. The molecular dynamics simulations suggest two mechanisms by which heat conductance was hindered: (i) abrupt bondlength mismatch in the contact zone edge due to the local stress field, which induces vibration mode competing and phonon scattering; (ii) extra structural deformation induced by tip-surface interlayer adsorption, which superimposes on the indentation-induced stress field, resulting in a clear thermal resistance boundary which can be significantly high for strong tip-surface interaction. Thermal conductivity and thermal conductance of indented GNR presents a flexible descending trend with respect to indentation depth, and Kapitza conductance changes significantly with respective tip-surface interaction strength. All the variations take place sensitively within a few to tens of angstroms length scale. Our study provides additional insight into the unique thermal properties of such interesting nanostructure and sheds new light on the application in the vicinity of thermal-transport-based new functional devices. One can envision that this kind of nanoscale, sensitive response of thermal transport versus local strain can be exploited for nanoscale sensing devices such as molecular sensor and position sensor.

Acknowledgements

We thank Dr Zheyong Fan and Dr Ning Wei for helpful discussions and comments. This work is supported by NSFC (No. 51202032), Program for Changjiang Scholars and Innovative Research Team in University (IRT1115), NSF of Fujian province (No. 2013J01009), and Program for the development of science and technology in Fujian province (No. 2012H0021).

Figures

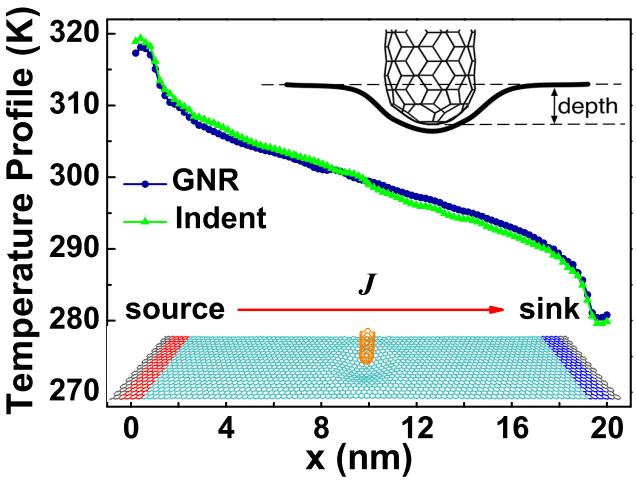

Fig. 1 (color on line) Sample temperature profiles of pristine GNR and indented GNR. The effective sample size is 20 nm $\times$ 5 nm, exclusive of the fixed regions and the thermobaths. The gray atoms at both ends are fixed; the red and blue atoms represent heat source and sink, respectively. A 5×5 capped CNT indents the graphene plane from the central point ($x \sim 10$ nm). The upper-right inset shows the definition of indentation depth. The line+circle and line+triangle curves show the temperature profiles of pristine GNR and indented GNR, respectively.

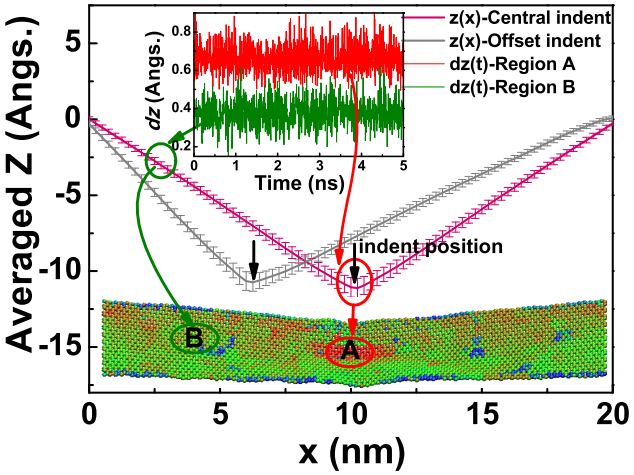

Fig. 2 (color on line) Vertical deflection profiles, represented as averaged z position vs ribbon length coordination x. To avoid the edge effect, only atoms in the central 10 $\AA$ of the ribbon (ribbon width is ~ 50 $\AA$) are analyzed. Error bars correspond to out-of-plane oscillation magnitude of atoms' z position. The red curve corresponds to the central indentation case (capped CNT indented on top of region A) and the grey curve corresponds to the case that indenter tip is shifted leftward. The lower inset snapshot illustrates the spatial atomic stress distribution, where the largest stress occurs at region A. The upper inset figure plots the out-of-plane displacement of z versus its average position at the time span for atoms in region A and B. It is interesting to notice that the largest oscillation occurs right beneath the tip.

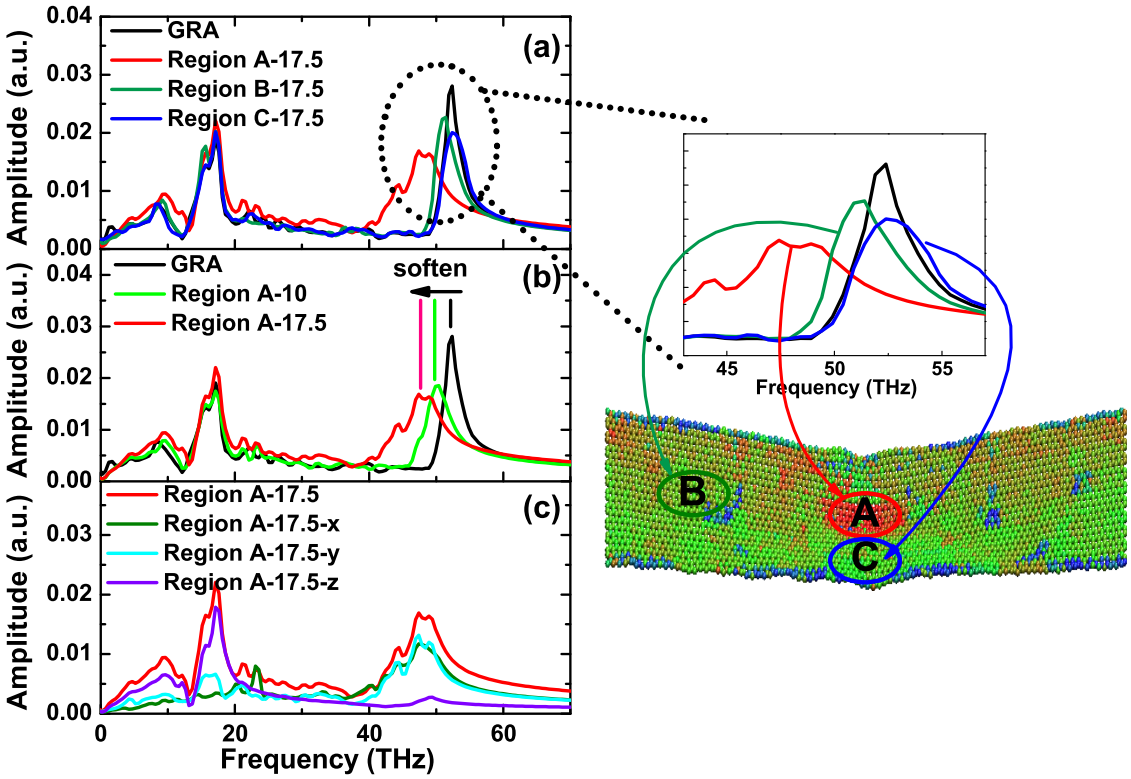

Fig. 3 (color on line) Comparison of phonon spectrums for pristine GNR and atoms over regions A, B, C in the indented GNR. The effective ribbon size is 20 nm × 5 nm. Region A locates right under the tip with the center coordinate of (10 nm,2.5 nm), region B locates at the left of region A with the center coordinate of (5 nm,2.5 nm), and region C locates at front of region A with the center coordinate of (10 nm,1.25 nm). The indentation depth of the tip is 17.5 Å. Curve for region A has a remarkable red-shift of the G-band. (b) Comparison of phonon spectrums for indented GNRs with different indentation depth, 10 *Å vs* 17.5 Å. The red-shift of the G-band is larger for deeper indentation. (c) Decomposition of the phonon spectrum for GNR with 17.5 *Å* indentation depth into its x, y, and z components. High frequency bands are contributed mainly by the in-plane vibrations and low frequency bands are contributed mainly by the off-plane vibrations.

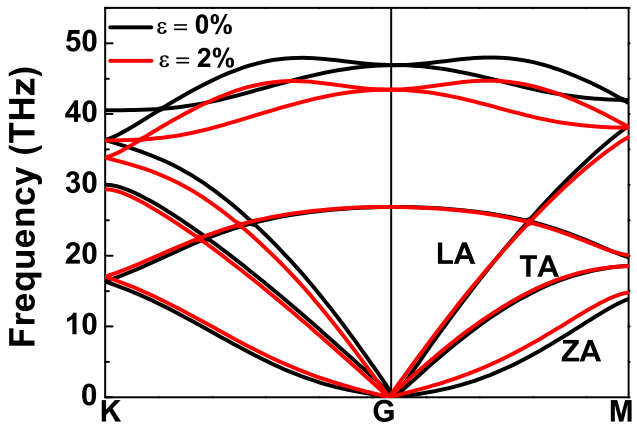

Fig. 4 (color on line) Phonon dispersion relations of unstrained graphene sheet (black) and of graphene sheet under uniform biaxial strain $\varepsilon = 2\%$ (red). Dispersion curves are computed from lattice dynamics calculations.

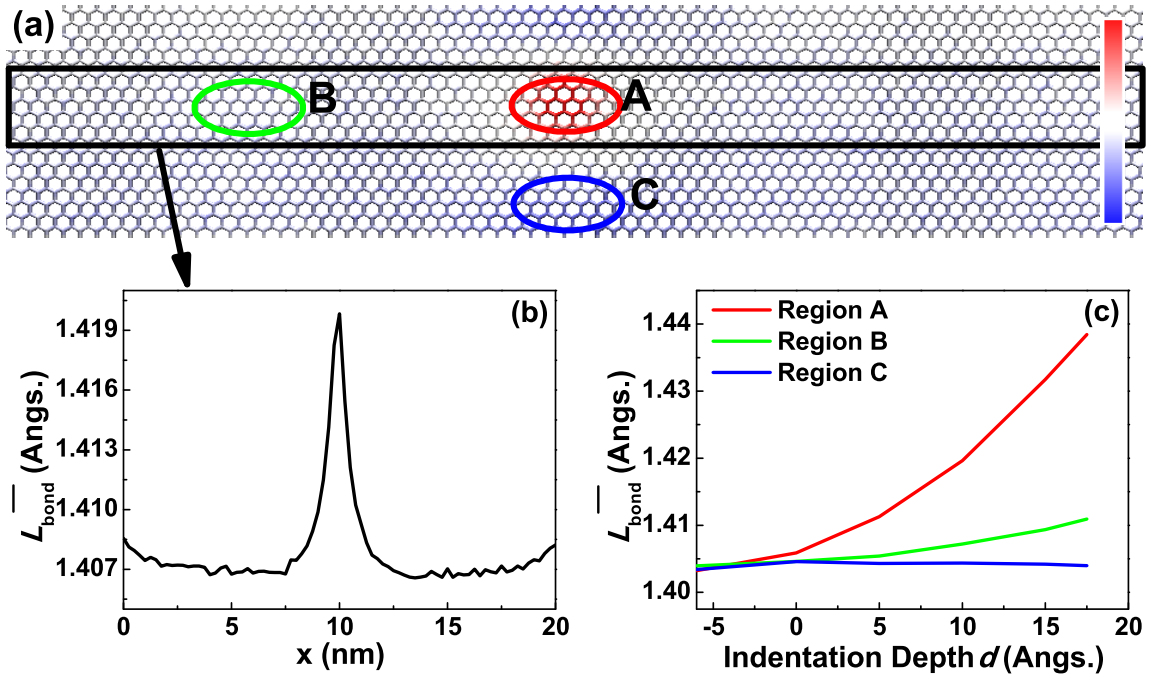

Fig. 5 (color on line) (a) Spatial distribution of the bond length for GNR with 10 $\AA$ indentation depth. Scale bar is shown at the right end. Bonds in region A are longest and bonds in region C are shortest. (b) The bond lengths in the black rectangle (middle portion of the ribbon) is averaged along y direction to give $\overline{L_{bond}(x)}$, which illustrates clearly that the longest bonds appear in region A. (c) Averaged bond length vs indentation depth in regions A, B and C. With deeper indentation, bond lengths in region A increase dramatically.

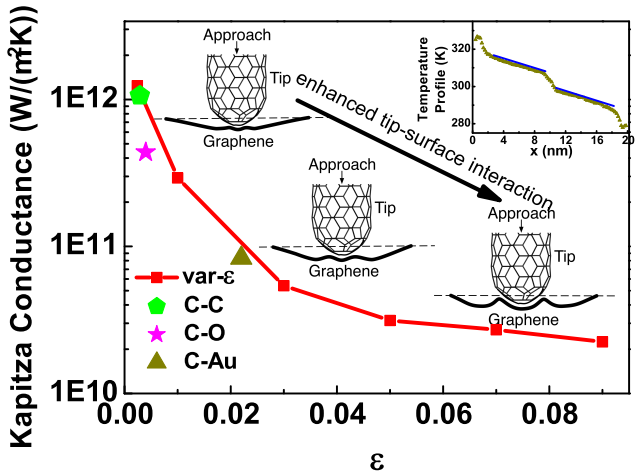

Fig. 6 (color on line) Kapitza conductance of indented region boundaries as a function of ε. Larger ε represents greater tip-surface interaction. The cut-off for data points in the line+square curve is set as 3.4 Å. Other parameters are listed in Table 1. The indentation depth is 10 Å. The upper-right inset shows a typical temperature profile for indented GNR with strong tip-surface interaction, where temperature jump at the indented position is obvious.

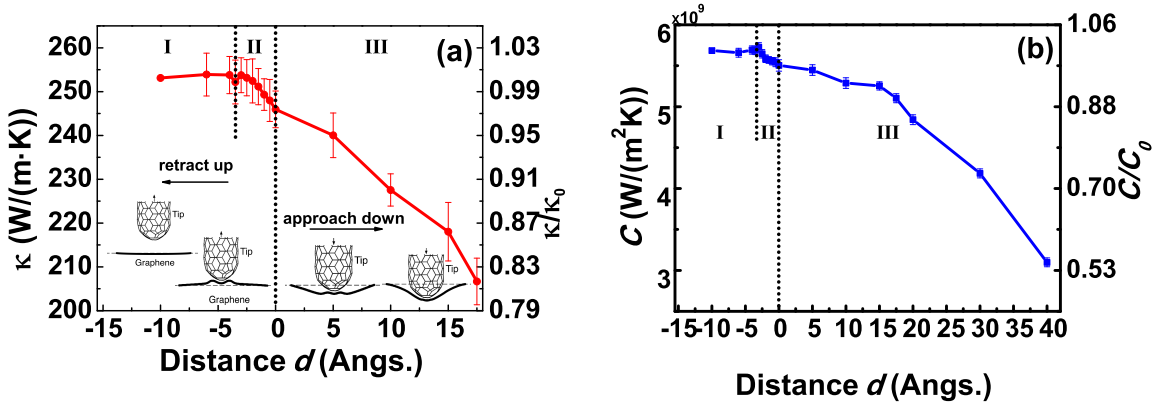

Fig. 7 (color on line) (a) Thermal conductivity κ and (b) thermal conductance C as a function of tip-surface distance d. Negative d corresponds to indentation (tip below the graphene basal plane) and positive d corresponds to lifting the GNR above its original surface height. The error bar is standard deviation obtained from ten independent runs. Regions I, II, and III correspond to non-interaction, adsorb, and indented regions, respectively. The right-y axis in (a) and (b) corresponds to the relative thermal conductivity κ/κ_0 and relative thermal conductance and C/C_0 respectively, where κ_0 and C_0 are taken from values of pristine GNR with the same size.

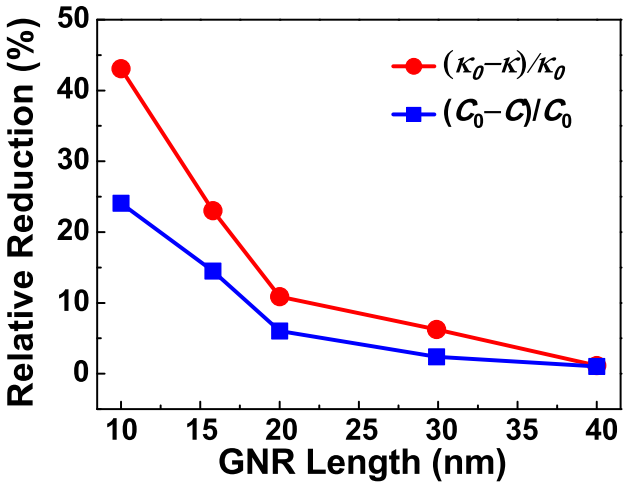

Fig. 8 (color on line) Relative reduction of (a) thermal conductivity $(\kappa_0 - \kappa)/\kappa_0$ and (b) thermal conductance $(C_0 - C)/C_0$ as a function of GNR length. The width is 50 Å, and the indentation depth is 15 Å for all the five investigated ribbons. κ_0 and C_0 are calculated from the corresponding pristine GNRs without indentation.

Tables

Table 1 Interaction coefficients between indenter tip and graphene surface. The tested tip elements include C, O, Au and arbitrary artificial element with varying ε.

	C-C[58]	C-O[59]	C-Au[60]	C-Artificial Element
ε (eV)	0.00296	0.00406	0.0220	0.0024$\sim$ 0.09
σ (Å)	3.3997	3.1900	2.7400	3.4000

Supplementary materials

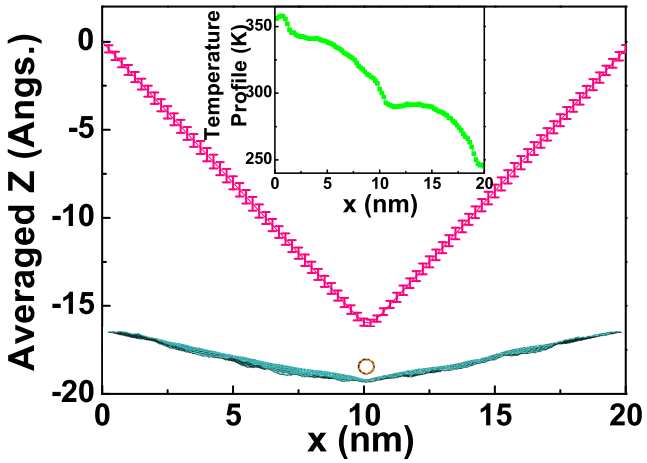

Fig. A1 (color on line) Vertical deflection profiles. The indented CNT lies across the plane and indented to a depth of 15 $\AA$, as showed in the lower inset snapshot. Error bars correspond to out-of-plane oscillation magnitude from the average height. The upper inset figure plots the temperature profile for the GNR.

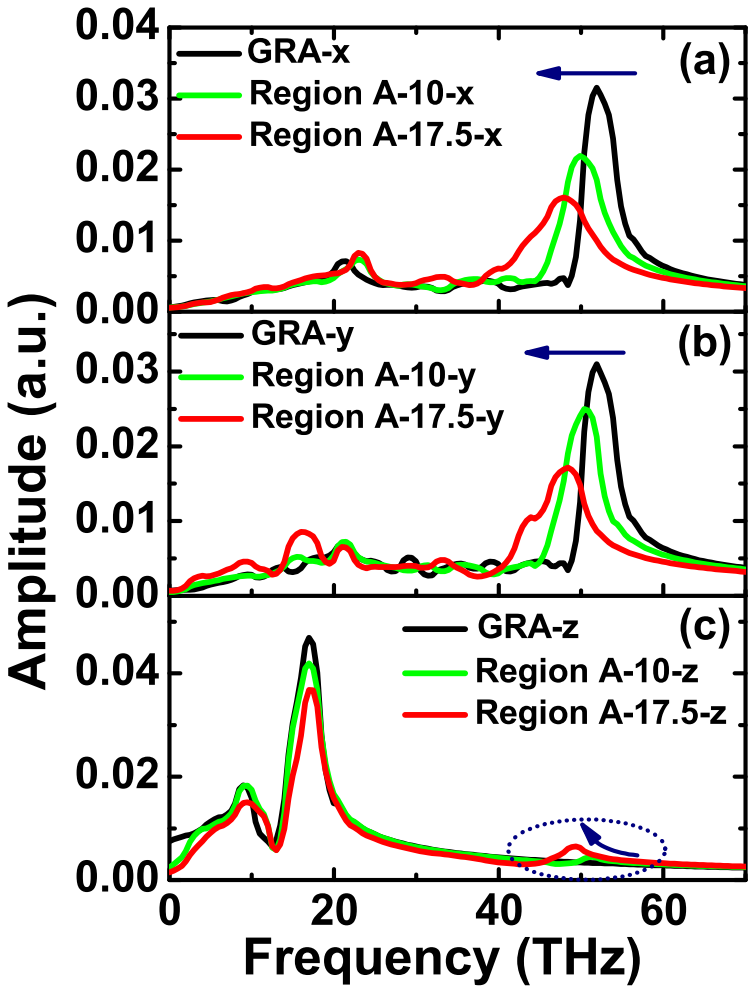

Fig. A2 (color on line) The x, y, z components of the phonon spectrums for pristine and indented GNR. Definition for region A is the same as that in Figure 3, and the indentation depth is 10 $\AA$ and 17.5 $\AA$, respectively.

References

1 K. S. Novoselov, Rev. Mod. Phys., 2011, **83**, 837–849.
2 C. Lee, X. D. Wei, J. W. Kysar and J. Hone, Science, 2008, **321**, 385–388.
3 A. A. Balandin, Nat. Materials, 2011, **10**, 569–581.
4 D. L. Nika and A. A. Balandin, J. Phys.: Condens. Matter, 2012, **24**, 233203.
5 A. A. Balandin, S. Ghosh, W. Bao, I. Calizo, D. Teweldebrhan, F. Miao and C. N. Lau, Nano Lett., 2008, **8**, 902–907.
6 S. Ghosh, I. Calizo, D. Teweldebrhan, E. P. Pokatilov, D. L. Nika, A. A. Balandin, W. Bao, F. Miao and C. N. Lau, Appl. Phys. Lett., 2008, **92**, 151911.
7 W. W. Cai, A. Moore, Y. Zhu, X. Li, S. Chen, L. Shi and R. S. Ruoff, Nano Lett., 2010, **10**, 1645–1651.
8 S. Chen, Q. Wu, C. Mishra, J. Kang, H. Zhang, K. Cho, W. Cai, A. A. Balandin and R. S. Ruoff, Nat. Mat., 2012, **11**, 203C207.
9 J. H. Seol, I. Jo, A. L. Moore, L. Lindsay, Z. H. Aitken, M. T. Pettes, X. Li, Z. Yao, R. Huang, D. Broido, N. Mingo, R. S. Ruoff and L. Shi, Science, 2010, **328**, 213–216.
10 K. L. Grosse, M.-H. Bae, F. Lian, E. Pop and W. P. King, Nat. Nanotech., 2011, **6**, 287–290.
11 C. Casiraghi, A. Hartschuh, H. Qian, S. Piscanec, C. Georgi, A. Fasoli, K. S. Novoselov, D. M. Basko and A. C. Ferrari, Nano Lett., 2009, **9**, 1433.
12 Y. W. Zhang, Q. X. Pei and C. M. Wang, Comput. Mater. Sci., 2012, **65**, 406–410.
13 X. Xu, L. F. C. Pereira, Y. Wang, J. Wu, a. X. Z. K. Zhang, S. Bae, C. T. Bui, R. Xie, J. T. L. Thong, B. H. Hong, K. P. Loh, D. Donadio, B. W. Li and B. O..zyilmaz, Nat. Commun., 2014, **5**, 3689.
14 M. Terraneo, M. Peyrard and G. Casati, Phys. Rev. Lett., 2002, **88**, 094302.
15 C. W. Chang, D. Okawa, H. Garcia, A. Majumdar and A. Zettl, Phys. Rev. Lett., 2007, **99**, 045901.
16 S. K. Chien and C. K. Yang, Y. T.and Chen, Appl. Phys. Lett., 2011, **98**, 033107.
17 J. Hu, X. Ruan and Y. P. Chen, Nano Lett., 2009, **9**, 2730C2735.
18 V. Varshney, S. S. Patnaik, A. K. Roy, G. Froudakis and B. L. Farmer, ACS Nano, 2010, **4**, 1153–1161.
19 X. Liu, G. Zhang and Y. W. Zhang, J. Phys. Chem. C, 2014, **118**, 12541–12547.
20 A. J. Lu, R. Q. Zhang and S. T. Lee, Appl. Phys. Lett., 2007, **91**, 263107.
21 K. F. Murphy, B. Piccione, M. B. Zanjani, J. R. Lukes and D. S. Gianola, Nano Lett., 2014.
22 Z. P. Xu and M. J. Buehler, Nanotechnology, 2009, **20**, 375704.
23 C. L. Ren, W. Zhang, Z. J. Xu, Z. Y. Zhu and P. Huai, J. Phys. Chem. C, 2010, **114**, 5786–5791.
24 X. Li, K. Maute, M. L. Dunn and R. Yang, Phys. Rev. B, 2010, **81**, 245318.
25 K. G. S. H. Gunawardana, K. Mullen, J. N. Hu, Y. P. Chen and X. L. Ruan, Phys. Rev. B, 2012, **85**, 245417.
26 J. Chen, J. H. Walther and P. Koumoutsakos, Nano Lett., 2014, **14**, 819–825.
27 N. Wei, L. Q. Xu, H.-Q. Wang and J.-C. Zheng, Nanotechnology, 2011, **22**, 105705.
28 F. Ma, H. B. Zheng, Y. J. Sun, D. Yang, K. W. Xu and P. K. Chu, Appl. Phys. Lett., 2012, **101**, 111904.
29 N. Bonini, J. Garg and N. Marzari, Nano Lett., 2012, **12**, 2673–2678.
30 N. N. Klimov, S. Jung, S. Zhu, T. Li, C. A. Wright, S. D. Solares, D. B. Newell, N. B. Zhitenev and J. A. Stroscio, Science, 2012, **336**, 1557–1562.
31 B. Zhan, C. Li, J. Yang, G. Jenkins, W. Huang and X. Dong, Small, 2014.
32 C. Chen, S. Rosenblatt, K. I. Bolotin, W. Kalb, P. Kim, I. Kymissis, H. L. Stormer, T. F. Heinz and J. Hone, Nature Nanotechnology, 2009, **4**, 861–867.
33 Y. Wang, L. Wang, T. Yang, X. Li, X. Zang, M. Zhu, K. Wang, D. Wu and H. Zhu, Adv. Funct. Mater., 2014, **24**, 4666–4670.
34 H. Choi, J. S. Choi, J.-S. Kim, J.-H. Choe, K. H. Chung, J.-W. Shin, J. T. Kim, D.-H. Youn, K.-C. Kim, J.-I. Lee, S.-Y. Choi, P. Kim, C.-G. Choi and Y.-J. Yu, Small, 2014.
35 B. Cho, J. Yoon, M. G. Hahm, D.-H. Kim, A. R. Kim, Y. H. Kahng, S.-W. Park, Y.-J. Lee, S.-G. Park, J.-D. Kwon, C. S. Kim, M. Song, Y. Jeong, K.-S. Nama and H. C. Ko, J. Mater. Chem. C, 2014, **2**, 5280–5285.
36 C. Lee, Q. Y. Li, W. Kalb, X. Z. Liu, H. Berger, R. W. Carpick and J. Hone, Science, 2010, **328**, 76–80.
37 S. Plimpton, J. Comput. Phys., 1995, **117**, 1–19.
38 S. J. Stuart, A. B. Tutein and J. A. Harrison, J. Chem. Phys., 2000, **112**, 6472.
39 W. G. Hoover, Phys. Rev. A, 1985, **31**, 1695.
40 P. Jude and R. Jullien, Phys. Rev. B, 1999, **59**, 13707.
41 J. Chen and H. Zhao, J Statistical Mechanics: Theory and Experiment,, 2012, **2012**, P06011.
42 J. M. Dickey and A. Paskin, Phys. Rev., 1969, **188**, 1407.
43 Z. Y. Ong and E. Pop, Phys. Rev. B, 2011, **84**, 075471.
44 J. W. Jiang, J. Chen, J. S. Wang and B. W. Li, Phys. Rev. B, 2009, **80**, 052301.
45 A. J. Gil, S. Adhikari, F. Scarpa and J. Bonet, J. Phys.: Condens. Matter, 2010, **22**, 145302.
46 N. Chandra, S. Namilae and C. Shet, Phys. Rev. B, 2004, **69**, 094101.
47 Q. X. Pei, Y. W. Zhang and V. B. Shenoy, Carbon, 2010, **48**, 898–904.
48 H. P. Li and R. Q. Zhang, Europhysics Lett., 2012, **99**, 36001.
49 O. Frank, G. Tsoukleri, J. Parthenios, K. Papagelis, I. Riaz, R. Jalil, K. S. Novoselov and C. Galiotis, ACSNano, 2010, **4**, 3131–3138.
50 L. F. C. Pereira and D. Donadio, Phys. Rev. B, 2013, **87**, 125424.
51 A. Bagri, S. P. Kim, R. S. Rouff and V. B. Shenoy, Nano Lett., 2011, **11**, 3917–3921.
52 Y. L. Wang, Z. G. Song and Z. P. Xu, J. Mater. Res., 2014, **29**, 362–372.
53 F. Hao, D. N. Fang and Z. P. Xu, Appl. Phys. Lett., 2012, **100**, 091903.
54 P. K. Schelling, S. R. Phillpot and P. Keblinski, J. Appl. Phys., 2004, **95**, 6082–6091.
55 V. Samvedi and V. Tomar, Nanotechnology, 2009, **20**, 365701.
56 Z. Deng, A. Smolyanitsky, Q. Y. Li, X. Q. Feng and R. J. Cannara, Nature Mater., 2012, **11**, 1032–1037.
57 L. Lindsay, W. Li, J. Carrete, N. Mingo, D. A. Broido and T. L. Reinecke, Phys. Rev. B, 2014, **89**, 155426.
58 L. A. Girifalco, M. Hodak and R. S. Lee, Phys. Rev. B, 2000, **62**, 13104.
59 T. Werder, J. H. Walther, R. L. Jaffe, T. Halicioglu and P. Koumoutsakos, J. Phys. Chem. B, 2003, **107**, 1345–1352.
60 L. J. Lewis, P. Jensen, N. Combe and J.-L. Barrat, Phys. Rev. B, 2000, **61**, 16084–16090.